Quantum Susceptibilities in Time-Domain Sampling of Electric Field Fluctuations

Matthias Kizmann, Andrey S. Moskalenko, Alfred Leitenstorfer, Guido Burkard, and Shaul Mukamel**

Electro-optic sampling has emerged as a new quantum technique enabling measurements of electric field fluctuations on subcycle time scales. In a second-order nonlinear material, the fluctuations of a terahertz field are imprinted onto the polarization properties of an ultrashort probe pulse in the near infrared. The statistics of this time-domain signal are calculated, incorporating the quantum nature of the involved electric fields right from the beginning. A microscopic quantum theory of the electro-optic process is developed adopting an ensemble of noninteracting three-level systems as a model for the nonlinear material. It is found that the response of the nonlinear medium can be separated into a conventional part, which is exploited also in sampling of coherent amplitudes, and quantum contributions, which are independent of the state of the terahertz input. Interactions between the three-level systems which are mediated by terahertz vacuum fluctuations are causing this quantum response. Conditions under which the classical response serves as a good approximation of the electro-optic process are also determined and how the statistics of the sampled terahertz field can be reconstructed from the electro-optic signal is demonstrated. In a complementary regime, electro-optic sampling can serve as a spectroscopic tool to study the pure quantum susceptibilities of matter.

1. Introduction

Nonlinear optics with laser light serves as one of the fundamental tools in modern experimental physics. In three-wave mixing spectroscopy, for example, materials are examined by irradiating them with optical fields and measuring the light emitted into a new direction. The spectral and temporal shape as well as the amplitude and phase of the incoming fields can be varied to study different effects. These options lead to a wide range of classical techniques such as, for example, coherent anti-Stokes Raman,[1] photon echo[2] and 2D femtosecond spectroscopy.[3] Exploiting strong coherent states of laser light justifies a classical treatment of the electric fields. The corresponding processes inside a material are then described by a classical response in terms of causal nonlinear susceptibilities.[4–6] Such a scenario involving quantum matter and classical fields underlies the area of classical nonlinear optics. In contrast to classical fields, quantum fields exhibit a larger number of degrees of freedom. This fact allows to exploit phenomena such as quantum superposition[7] and entanglement[8,9] in order to enhance classical spectroscopic tools.[10]

Usually, the nonlinear susceptibilities are calculated separately from the electric fields involved and then inserted into an effective Hamiltonian describing the nonlinear interaction.[5,6] This description requires that all light fields remain in a classical limit and correlations between them may be neglected. Theories relying on effective Hamiltonians can also accurately describe the interaction between quantum fields and nonlinear matter in an off-resonant regime. Nonlinear processes such as four-wave mixing[11] or parametric downconversion[12–14] far from resonance are typically exploited to generate nonclassical states of light. In the vicinity of resonant transitions, the classical susceptibilities alone fail to accurately describe the response of nonlinear matter to quantum fields. Here, the physics is most adequately described by quantum susceptibilities that are influenced by higher-order fluctuations of the nonlinear medium.[15–17]

In its standard application, electro-optic sampling represents a typical example for classical nonlinear optics. Here, a short near-infrared probe pulse is used to sample the trace of a classical terahertz (THz) transient with subcycle temporal resolution.[18–20] The fields interact in a second-order $\chi^{(2)}$ nonlinear crystal and the polarization of the near-infrared probe changes proportionally to the local THz amplitude. This technique was recently extended into the quantum domain by applying it to THz fields with vanishing mean values such as, for example, vacuum fluctuations.

M. Kizmann, A. Leitenstorfer, G. Burkard
Department of Physics and Center for Applied Photonics
University of Konstanz
Konstanz D-78457, Germany

A. S. Moskalenko
Department of Physics
KAIST
Daejeon 34141, Republic of Korea
E-mail: moskalenko@kaist.ac.kr

S. Mukamel
Department of Chemistry and Physics and Astronomy
University of California
Irvine, CA 92697-2025, USA
E-mail: smukamel@uci.edu

The ORCID identification number(s) for the author(s) of this article can be found under https://doi.org/10.1002/lpor.202100423

DOI: 10.1002/lpor.202100423
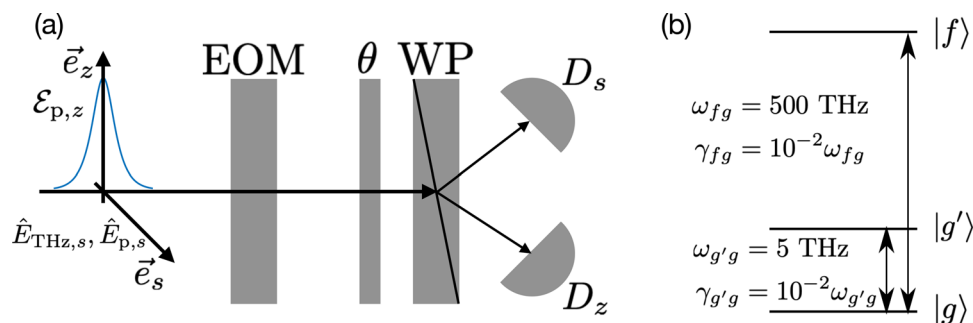
Figure 1. Setup for electro-optic sampling and level scheme of the molecules constituting the nonlinear medium. a) Experimental setup consisting of a nonlinear electro-optic medium (EOM), a waveplate inducing a phase shift of θ along its fast axis, a Wollaston prism (WP) separating the two polarization directions and two photon detectors D_s and D_z. An intense $\vec{e}_z$-polarized coherent near-infrared (NIR) probe pulse (blue) $\mathcal{E}_{p,z}$ is applied to probe a co-propagating quantum THz field $\hat{E}_{THz,s}$ polarized in the perpendicular $\vec{e}_s$ direction. $\hat{E}_{p,s}$ denotes the induced $\vec{e}_s$-polarized NIR quantum field. b) Model for the molecules representing the EOM, comprising three levels $i, j = g, g', f$ with transition frequencies ω_{ij} and lifetime broadenings γ_{ij}.

The probe is sampling the statistics of the input on subcycle time scales by imprinting it onto its polarization state.[21,22] The striking advantage of electro-optic sampling in comparison to standard homodyne detection[23] relies on providing information on the fluctuations of THz fields directly in the time domain, in complete analogy to its classical counterpart.[24–26] A slightly extended configuration also allows to characterize the spatio-temporal correlations of THz fields[22,27] and might provide a useful spectroscopic tool to access, for example, the linear dielectric function of materials without requiring any incoming photons.[28] Theoretical models have so far relied on a macroscopic description of the second-order nonlinear interaction inside the crystal based on a classical susceptibility $\chi^{(2)}$.[29,30] Here, the sampling of a classical THz field is straightforwardly extended to the quantum regime. We investigate the limitations of this approach and demonstrate when quantum effects of the nonlinear response must be taken into account.

To this end, a time-domain quantum electrodynamic theory of electro-optic sampling is developed. A system of three-level noninteracting molecules is employed to model the nonlinear medium and to calculate its frequency response in amplitude and phase. We demonstrate how fluctuations of the phase-dependent quadratures of the generated electro-optic signal can be measured and that a full quantum tomography of the generated signal is feasible. Our theory focuses on the nature of the nonlinear electro-optic response and pinpoints under which conditions a straightforward reconstruction of the quantum fluctuations is possible. Two types of quantum corrections are identified: quantum susceptibilities and cascading processes which lead to an effective intermolecular interaction mediated by THz fluctuations. Previous theories[29,30] did not include these effects. We show that the ultrashort temporal duration of the probe pulse leads to time-ordering for the cascading processes that squeeze the generated near-infrared field for certain phase shifts. Conditions under which electro-optic sampling might be employed as a spectroscopic tool to study quantum susceptibilities are explored. Finally, we describe how the probability distribution of the bare THz fluctuations can be reconstructed from the measured probability distribution of the electro-optic signal and find that quantum corrections can affect this reconstruction.

2. The Setup

The geometry of the setup and the level scheme exploited to describe the nonlinear medium are sketched in **Figure 1**a,b, respectively.

We assume an effective three-level electro-optic medium (EOM), depicted in Figure 1b that exhibits a second-order nonlinear susceptibility tensor with a zincblende-type symmetry. The EOM is modeled by a large number of independent quantum systems which we term molecules. An intense near-infrared (NIR) probe field in a strong multimode coherent state $|\{\mathcal{E}_{p,z}\}\rangle$ with a large amplitude $\mathcal{E}_{p,z}(\omega) = \langle\{\mathcal{E}_{p,z}\}|\hat{E}_{p,z}(\omega)|\{\mathcal{E}_{p,z}\}\rangle$ and a terahertz (THz) field $\hat{E}_{THz,s}()$ are sent into the EOM. These beams are linearly polarized along the $\vec{e}_z$ and $\vec{e}_s$ directions, respectively. While propagating through the nonlinear medium, the two fields undergo sum- (SFG) and difference-frequency generation (DFG). Both three-wave mixing processes generate an $\vec{e}_s$-polarized weak contribution to $\hat{E}_{p,s}$. A waveplate then shifts the two polarization components of the NIR field after the EOM by the angle θ with respect to each other, effectively mixing the two contributions (see Section S1, Supporting Information). The light is then sent through a Wollaston prism which separates the two polarization directions. Finally, the number of photons in these beams, $\hat{N}'_s$ and $\hat{N}'_z$, are measured with the detectors D_s and D_z, respectively. The electro-optic signal is defined by their difference,

$$\hat{S}(\theta) = \hat{N}'_z - \hat{N}'_s = C \int_0^\infty d\omega \frac{1}{\hbar\omega} \left[P(\theta)\hat{E}^\dagger_{p,z}(\omega)\hat{E}_{p,s}(\omega) + \text{H.c.} \right] \quad (1)$$

where $C = 4\pi\varepsilon_0 A c_0$ with A being the effective transverse area determined by the beam waist of the probe field, c_0 the speed of light in vacuum, ε_0 the vacuum permittivity and $P(\theta) = \sqrt{-\cos\theta} + i\sqrt{2}\cos(\theta/2)$. A phase shift by $\theta = \pi/2$ or $\theta = \pi$ is induced by a quarter- or half-wave plate, respectively[31] (see Figure 1a).

The mean value of the electro-optic signal $\hat{S}(\theta)$ is proportional to that of the sampled THz field.[18,32–34] The temporal profile of an electrical transient can therefore be sampled by measuring the mean value of $\hat{S}(\theta)$ for different delay times between the probe and the THz field. To achieve subcycle temporal resolution, the NIR probe field must be shorter than the characteristic period

of the input field. To gain insight into the quantum character of light, higher moments of the electric field are of interest.[21,29,30,35] To access them experimentally, the statistics of $\hat{S}(\theta)$ needs to be collected. The relative likelihood of each measurement result S builds up a histogram representing the probability distribution $P(S, \theta)$ equivalently to standard balanced homodyne tomography. Theoretically, $P(S, \theta)$ is given by (see Section S1, Supporting Information)

$$
\begin{aligned}
P(S, \theta) &= \left\langle : \frac{1}{\sqrt{2\pi N}} e^{-\frac{(S - \hat{S}(\theta))^2}{2N}} : \right\rangle \\
&= \frac{1}{\sqrt{2\pi N}} \sum_{k=0}^{\infty} \frac{1}{(2N)^{k/2} k!} H_k\left(S/\sqrt{2N}\right) \\
&\quad \times \exp\left(-\frac{S^2}{2N}\right) \left\langle : \hat{S}^k(\theta) : \right\rangle
\end{aligned}
\tag{2}
$$

where $N = C \int_0^{\infty} d\omega |\mathcal{E}_{p,z}(\omega)|^2 / \hbar\omega$ is the mean number of photons of the probe, $H_k(x)$ is the kth-order Hermite polynomial and the colons denote normal ordering.

3. Superoperator Representation of Classical and Quantum Nonlinear Susceptibilities

In this work, we want to ignore corrections to the probability distribution related to the mean value of the signal $\langle : \hat{S}(\theta) : \rangle$ since they only provide information about the classical characteristics of the THz input. Instead, we focus on the normally-ordered second moment of the signal, $°C = \langle : \hat{S}^2(\theta) : \rangle$. The variance of $\hat{S}(\theta)$ is given by $\langle \hat{S}^2(\theta) \rangle = N + °C$, where N is the shot noise of the probe. Moreover, we consider the sampling of THz vacuum fluctuations since they represent a natural resource in the experiment and the physics remains maximally transparent. An expression for $°C$ that describes the sampling of arbitrary quantum fields is derived in Section S2, Supporting Information. We employ the superoperator formalism[4] which offers a compact quantum treatment of both the matter system and the electric fields to derive a microscopic expression for $°C$. Within this framework, we associate plus- and minus-type superoperators with any ordinary operator $\hat{A}$ which are defined by their action on an arbitrary operator $\hat{X}$; $\hat{A}_+ \hat{X} = \frac{1}{2}\{\hat{A}, \hat{X}\} = \frac{1}{2}(\hat{A}\hat{X} + \hat{X}\hat{A})$ and $\hat{A}_- \hat{X} = [\hat{A}, \hat{X}] = \hat{A}\hat{X} - \hat{X}\hat{A}$. The evolution of the system is determined by the dipole light-matter interaction Hamiltonian $H_{int}(t) = -\sum_{\alpha=z,s} \int_V d^3r \, \hat{\varepsilon}_\alpha(\vec{r}, t) \hat{V}_\alpha(t)$ where V denotes the volume of the electro-optic medium. The corresponding superoperator $\hat{H}_{int,-}(t)$ is given by[15]

$$
\hat{H}_{int,-}(t) = -\sum_{\alpha=z,s} \int_V d^3r \, \left[\hat{\varepsilon}_{\alpha,+}(\vec{r}, t)\hat{V}_{\alpha,-}(t) + \hat{\varepsilon}_{\alpha,-}(\vec{r}, t)\hat{V}_{\alpha,+}(t)\right]
\tag{3}
$$

where we have used the fact that the dipole and the electric field operators commute. Here, $\alpha = z, s$ represents the two possible mutually perpendicular polarizations, $\hat{\varepsilon}_\alpha(\vec{r}, t) = \hat{E}_{p,\alpha}(\vec{r}, t) + \hat{E}_{THz,\alpha}(\vec{r}, t) + \text{H.c.}$ is the sum of all relevant field modes and $\hat{V}_\alpha(t) = \hat{V}_\alpha(t) + \hat{V}_\alpha^\dagger(t)$ denotes the dipole operator in the interac-

tion picture with $\hat{V}_\alpha = \mu_{\alpha,gg'}|g\rangle\langle g'| + \mu_{\alpha,gf}|g\rangle\langle f| + \mu_{\alpha,g'f}|g'\rangle\langle f|$ and $\mu_{\alpha,ij}$ as the dipole moment for the $j \to i$ transition ($i, j = g, g', f$).

The normally-ordered second moment of the electro-optic signal $°C$ is calculated from the time-dependent density matrix of the entire system of field and matter $\hat{\rho}$

$$
°C \equiv \langle : \hat{S}^2(\theta) : \rangle = \text{tr}\left\{ : \hat{S}^2(\theta) : \mathcal{T} \exp\left(-\frac{i}{\hbar} \int_{-\infty}^{\infty} dt \hat{H}_{int,-}(t)\right) \hat{\rho}_{in} \right\}
\tag{4}
$$

Here, $\hat{\rho}_{in} = \hat{\rho}_{field} \otimes \hat{\rho}_{mat}$ denotes the initial density matrix given by a direct product of the density matrices for field and matter and $\mathcal{T}$ represents the time-ordering operator for the superoperators. We assume $\hat{\rho}_{field} = |\{\mathcal{E}_{p,z}\}\rangle\langle\{\mathcal{E}_{p,z}\}| \otimes |0_s\rangle\langle 0_s|$, that is, the electric field consists of a multimode coherent state in the $\vec{e}_z$-polarized NIR range and the electromagnetic vacuum in both the $\vec{e}_s$-polarized NIR and THz ranges. The matter system consists of an ensemble of noninteracting molecules initially in the ground state. Since the trace operation is invariant under cyclic permutation, we can let the time evolution according to the interaction Hamiltonian in Equation (3) act on $: \hat{S}^2(\theta) :$. The trace can then be factorized into a product of traces over the field and the matter degrees of freedom. The matter trace is given by a time-ordered product of n Green's functions of superoperators for the $(n + 1)$th-order perturbation term in $\hat{H}_{int,-}(t)$, resulting in the nth-order susceptibility.

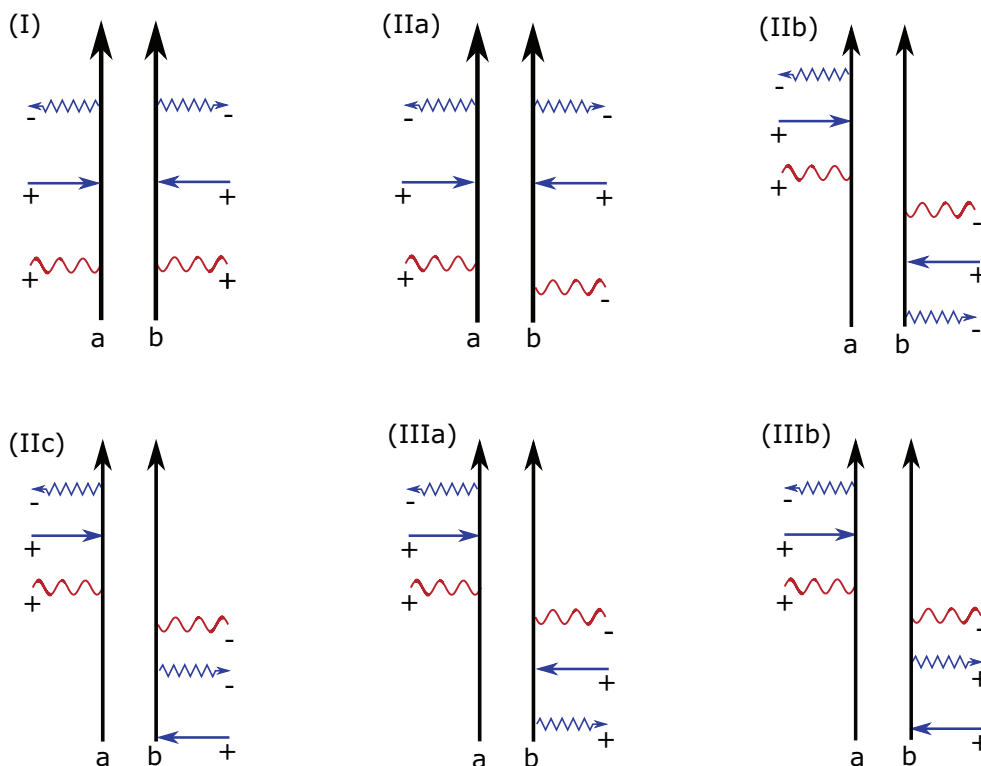We define the second-order susceptibility

$$
\begin{aligned}
\chi_{+rs}^{(2)}\left(-(\omega_2 + \omega_1); \omega_2, \omega_1\right) &= \frac{1}{\varepsilon_0 \hbar^2} \int_0^{\infty} \int_0^{\infty} dt_2 dt_1 e^{i\omega_2 t_1} e^{i\omega_1(t_1 + t_2)} \\
&\quad \times \text{Tr}\left\{ \hat{V}_+(0)\hat{V}_r(-t_1)\hat{V}_s(-t_1 - t_2) \hat{\rho}_{mat} \right\}
\end{aligned}
\tag{5}
$$

where $r, s = \pm$ indicate the type of superoperator dipole operators and the subscript $(+rs)$ denotes the sequence of the time-ordered superoperators of the dipole operators $\hat{V}(t)$ (an explicit formula for the susceptibilities is given in Section S2, Supporting Information). Note that the last interaction with the dipole operator has to be of the "+" type since the expectation value in Equation (5) would otherwise be given by a trace over a commutator which vanishes due to the invariance of the trace under cyclic permutation. Earlier interactions can be of either the "+" or the "−" type. They are accompanied by the opposite superoperator interaction for the corresponding field [see Equation (3)]. The various sequences of superoperator interactions can be used to differentiate between classes of second-order susceptibilities.

Usually, nonlinear susceptibilities are calculated assuming interaction with classical electric fields. Second-order processes lead to a classical susceptibility of the form $\chi_{+--}^{(2)}$, that is, n "−"-type dipole operator interactions, followed by a "+"-type interaction for the nth-order susceptibility. Accordingly, the sequence of superoperator interactions for the fields is given by its conjugate (n "+"-type and one "−"-type interaction). These types of susceptibilities are also denoted causal since the matter system interacts with two fields (first two "+"-type interactions) and generates a new field (last "−"-type interaction). Another class of second-order susceptibilities is given by $\chi_{++-}^{(2)}$ where the corresponding sequence of superoperator interactions for the electric fields is $(- - +)$. Here, the nonlinear medium first

ADVANCED
SCIENCE NEWS

www.advancedsciencenews.com

LASER
& PHOTONICS
REVIEWS

www.lpr-journal.org

Figure 2. Diagrams representing the leading contributions to electro-optic sampling of THz vacuum fluctuations [Equation (6)] for two molecules *a* and *b*. Each diagram depicts interactions between the electric field modes and the density matrix of the matter system. The vertical arrows indicate the time evolution of molecules *a* and *b* from the past (bottom) to the present (top), respectively. The red wavy lines denote an interaction with either $\hat{E}_{\text{THz},s}$ or $\hat{E}^{\dagger}_{\text{THz},s}$, the blue zigzag arrows pointing to the left (right) represent interactions with $\hat{E}^{\dagger}_{p,s}$ ($\hat{E}_{p,s}$) and the straight blue arrows pointing to the left (right) denote interactions with the coherent probe field $\mathcal{E}^{*}_{p,z}$ ($\mathcal{E}_{p,z}$), respectively. The $\pm$ signs next to the horizontal arrows denote the type of superoperator interaction for the corresponding field mode. I) A process that can be described by classical susceptibilities. This diagram is the only one captured by the classical treatment. IIa–c) Processes that involve quantum susceptibilities due to two "−"-type interactions of molecule *b* with $\hat{E}_{p,s}$ and $\hat{E}_{\text{THz},s}$. IIIa,b) Cascading processes that can be described by classical susceptibilities but are not captured by the classical treatment described in the main text. The diagrams depicted here survive the rotating wave approximation (RWA). For a detailed calculation and the full set of diagrams see Section S2, Supporting Information.

interacts with the field mode associated with the respective "−"-type dipole operator interaction and then generates two fields through spontaneous fluctuations described by the two "+"-type dipole operator interactions. No clear time ordering for the generation of the two fields can be established. Therefore, this susceptibility as well as any kind of susceptibilities with more than one "−"-type interaction for the fields should be denoted quantum or noncausal susceptibilities.[17]

4. Normally-Ordered Second Moment of the THz Vacuum Field

In this section, we calculate the normally-ordered second moment °C. Since both the NIR $\hat{E}_{p,s}$ and the THz $\hat{E}_{\text{THz},s}$ field modes are initially in the vacuum state, each of them must interact at least twice to give a nonvanishing contribution to Equation (4). Therefore, we need to have two interactions with $\hat{E}_{p,z}$, $\hat{E}_{p,s}$, and $\hat{E}_{\text{THz},s}$, each. It is now mandatory to expand the exponential in Equation (4) to sixth order in $\hat{H}_{\text{int},-}$. Linear contributions may

be neglected. Due to the large number of molecules, the dominant contribution to the signal comes from pairs of molecules each interacting three times with the dipole operator. We are thus considering two second-order processes instead of a single fifth-order process. The probe will be treated classical because of its strong coherent amplitude, that is, we only take into account interactions of the form $\hat{E}_{p,z,+}$ since $\hat{E}_{p,z,-}$ vanishes for a classical field. This approximation does not apply to the quantum fields $\hat{E}_{p,s}$ and $\hat{E}_{\text{THz},s}$. The leading diagrams for °C that survive the rotating wave approximation (RWA) are given in **Figure 2**. Note that the RWA has not been applied in our calculations which are based on Equation (3) and include the full set of diagrams given in Section S2, Supporting Information. In Figure 2I, the pair of molecules that generate the signal interact with the THz vacuum through $\hat{E}_{\text{THz},s,+}$. In this case, the time ordering of these two interactions is immaterial and the nonlinear processes are completely independent of each other. In contrast, the remaining diagrams describe shared fluctuations between two molecules that involve the commutator of two THz field modes. The first interaction with $\hat{E}_{\text{THz},s,-}$ on molecule *b*, for example, emits a THz photon
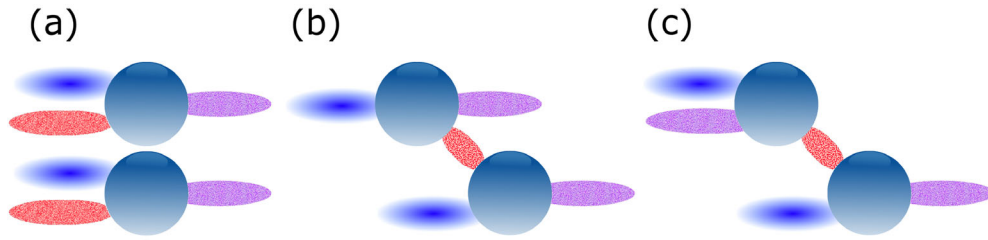
Figure 3. Visualization of the three different types of responses. a) The probe $\mathcal{E}_{p,z}$ (blue) and the THz vacuum $\widehat{E}_{THz,s}$ (red) interact with two molecules (spheres) to generate the NIR field $\widehat{E}_{p,s}$ (violet). The two processes happen independently of each other and belong to the classical response ff_I in Equation (7). b) The probe interacts with one molecule to generate both a THz and a NIR field. The generated THz field together with the probe then interacts with a second molecule to generate an additional NIR field. The first $\chi^{(2)}$ process is described by quantum susceptibilities and the response is given by Equation (9). c) The probe and the NIR vacuum interact with one molecule to generate a THz field. The generated THz component together with the probe then interacts with a second molecule to generate a NIR field. These are cascading processes which are described by Equation (11).

which is then absorbed by molecule a through the interaction with $\widehat{E}_{THz,s,+}$. Therefore, the intermolecular time ordering of these interactions with the THz field is crucial. It leads to an effective interaction between molecules a and b that is mediated by the THz vacuum fluctuations. These processes can only be understood in the joint space of both molecules. We note that initially and in the final state, all molecules are uncoupled. The coupling exists during the interaction process initiated by the probe field, where an excited molecule can transfer its excitation to another molecule via the THz vacuum. No classical field is generated at any point during this process. We split the normally-ordered second moment $°C$ of the electro-optic signal into three contributions

$$°C = °C_I + °C_{II} + °C_{III} \tag{6}$$

which will be discussed in detail below.

The first contribution $°C_I$ is given by

$$°C_I = \left(\frac{N\omega_p L}{c_0}\right)^2 \int_0^\infty d\frac{\hbar}{C} \left[1 + \text{sinc}^2\left(2L/c_0\right)\right] |D(,\theta)|^2 \tag{7}$$

where $\omega_p = \int_0^\infty d\omega |\mathcal{E}_{p,z}(\omega)|^2 / \int_0^\infty d\omega (1/\omega)|\mathcal{E}_{p,z}(\omega)|^2$ is the average detected frequency and L is the length of the nonlinear medium along the propagation direction. In the following, ω and denote frequencies in the NIR and THz range, respectively. We have further introduced the gating function $D(,\theta)$ which depends on the classical susceptibilities $\chi^{(2)}_{+--}$

$$
\begin{aligned}
D(,\theta) = &\frac{1}{2}\int_0^\infty d\omega f_+^*(\omega,,\theta) \\
&\times \left(\chi^{(2)*}_{+--}(-\omega;-,\omega+) + \chi^{(2)*}_{+--}(-\omega;\omega+,-)\right) \\
&-\frac{1}{2}\int_0^\infty d\omega f_-(\omega,,\theta) \\
&\times \left(\chi^{(2)}_{+--}(-\omega;,\omega-) + \chi^{(2)}_{+--}(-\omega;\omega-,)\right)
\end{aligned} \tag{8}
$$

with the autocorrelation functions $f_\pm(\omega,,\theta) = P(\theta)\mathcal{E}_{p,z}^*(\omega)\mathcal{E}_{p,z}(\omega\pm)/\int_0^\infty d\omega |\mathcal{E}_{p,z}(\omega)|^2$. The leading diagram to this contribution is depicted in Figure 2I. Here, both molecules interact independently with the THz vacuum and the matter response can be described in the single-molecule space. In that sense, the THz vacuum may be treated as a classical field in analogy to the

response of conventional electro-optic sampling which is why the matter response is given by classical susceptibilities $\chi^{(2)}_{+--}$ [cf. Equation (5)]. **Figure 3**a provides a visual representation of these processes. The same result may be also obtained by calculating the third-order correction to the electro-optic signal $\widehat{S}(\theta)$ in Equation (1) and squaring it [see the result for arbitrary THz fields in Equation (B7) of Section S2, Supporting Information]. $°C_I$ represents the classical contribution to the normally-ordered second moment $°C$ and always remains positive. These are the only processes that depend on the state of the THz field and are actually sampling its fluctuations [cf. Equation (B7) in Section S2, Supporting Information]. We thus have a quantum extension of classical electro-optic sampling which not only provides access to the temporally resolved mean value of the THz input but also its fluctuations.

The other two contributions $°C_{II}$ and $°C_{III}$ in Equation (6) constitute genuine quantum corrections. Here, the first interaction of the matter system with the THz field is given by the superoperator $\widehat{E}_{THz,s,-}$, generating a THz field which propagates further and interacts with a second molecule according to $\widehat{E}_{THz,s,+}$. This process leads to an intermolecular time ordering of the two $\chi^{(2)}$ processes and an effective intermolecular interaction which is only understandable in the two-molecule space. The intermolecular time ordering is reflected in interference terms that may also reduce the fluctuations of the electro-optic signal. Contributions of this type involve the commutator of the THz field operators and are independent of their state. They therefore represent byproducts of the nonlinear interaction that do not provide any information on the THz input.

$°C_{II}$ is given by

$$
\begin{aligned}
°C_{II} = &\left(\frac{N\omega_p L}{c_0}\right)^2 \int_0^\infty d\frac{\hbar}{C} \left[1 + \text{sinc}^2\left(2L/c_0\right)\right] \\
&\times \Re\left\{D(,\theta)D_q(,\theta)\right\} \\
&-\left(\frac{N\omega_p L}{c_0}\right)^2 \int_0^\infty d\frac{\hbar c_0}{CL} \left[3 + \text{sinc}^2\left(2L/c_0\right)\right] \\
&\times \Im\left\{D(,\theta)D_q(,\theta)\right\}
\end{aligned} \tag{9}
$$

where $\Re\{\cdot\}$ and $\Im\{\cdot\}$ denote the real and imaginary part, respectively. Here, the classical gating function $D(,\theta)$ is given in

Equation (8) and the gating function $D_q(,\theta)$, which depends on quantum susceptibilities, is given by

$$
\begin{aligned}
D_q(,\theta) = &\int_0^\infty d\omega f_+(\omega,,\theta) \\
&\times \left(\chi^{(2)}_{++-}(-;-\omega,\omega+) + \chi^{(2)}_{+-+}(-;\omega+,-\omega) \right) \\
&+ \int_0^\infty d\omega f_+(\omega,,\theta) \\
&\times \left(\chi^{(2)}_{++-}(-\omega;-,\omega+) + \chi^{(2)}_{+-+}(-\omega;\omega+,-) \right) \\
&+ \int_0^\infty d\omega f_-^*(\omega,,\theta) \\
&\times \left(\chi^{(2)*}_{++-}(;-\omega,\omega-) + \chi^{(2)*}_{+-+}(;\omega-,-\omega) \right) \\
&+ \int_0^\infty d\omega f_-^*(\omega,,\theta) \\
&\times \left(\chi^{(2)*}_{++-}(-\omega;,\omega-) + \chi^{(2)*}_{+-+}(-\omega;\omega-,) \right)
\end{aligned}
\tag{10}
$$

D_q involves quantum susceptibilities of the form $\chi^{(2)}_{++-}$ and $\chi^{(2)}_{+-+}$ [cf. Equation (5)]. Figure 3b demonstrates these types of processes. The leading diagrams are depicted in Figure 2IIa–c. Observing features related to these susceptibilities therefore assures that a genuinely nonclassical field was involved in the responsible nonlinear process.

Finally, $°C_{III}$ is given by

$$
\begin{aligned}
°C_{III} = &\left(\frac{N\omega_p L}{c_0} \right)^2 \int_0^\infty d\frac{\hbar}{C} \left[1 + \text{sinc}^2 (2L/c_0) \right] \\
&\times \Re \{ D(,\theta) D_{casc}(,\theta) \} \\
&- \left(\frac{N\omega_p L}{c_0} \right)^2 \int_0^\infty d\frac{\hbar c_0}{CL} \left[3 + \text{sinc}^2 (2L/c_0) \right] \\
&\times \Im \{ D(,\theta) D_{casc}(,\theta) \}
\end{aligned}
\tag{11}
$$

where the gating function $D_{casc}(,\theta)$ which depends on the classical susceptibilities $\chi^{(2)}_{+--}$ is given by

$$
\begin{aligned}
D_{casc}(,\theta) = &\frac{1}{2} \int_0^\infty d\omega f_+(\omega,,\theta) \\
&\times \left(\chi^{(2)}_{+--}(-;-\omega,\omega+) + \chi^{(2)}_{+--}(-;\omega+,-\omega) \right) \\
&+ \frac{1}{2} \int_0^\infty d\omega f_-^*(\omega,,\theta) \\
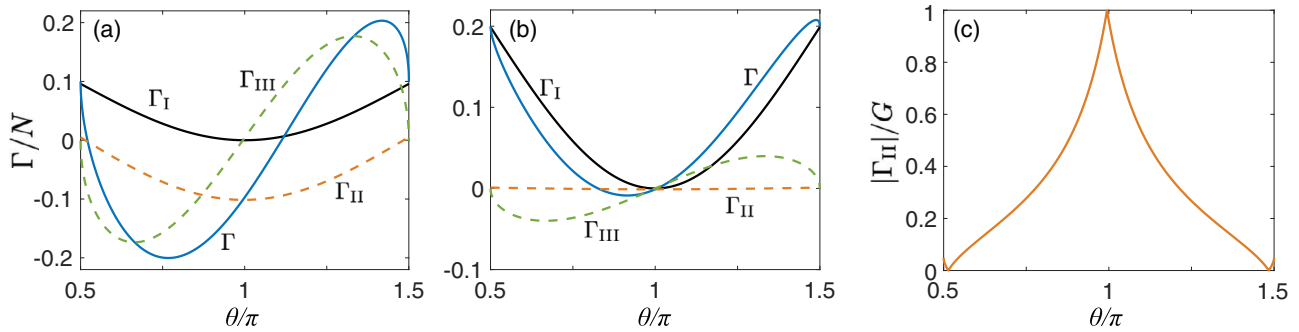&\times \left(\chi^{(2)*}_{+--}(;-\omega,\omega-) + \chi^{(2)*}_{+--}(;\omega-,-\omega) \right)
\end{aligned}
\tag{12}
$$

$°C_{III}$ constitutes a quantum correction even though the gating function $D_{casc}(,\theta)$ only involves classical susceptibilities of the type $\chi^{(2)}_{+--}$. Here, we deal with cascading processes where for example a photon is emitted into the THz vacuum by molecule b and then reabsorbed at molecule a. Figure 3c gives a visual representation of this kind of processes. The leading diagrams are shown in Figure 2IIIa,b. The cascading processes can also be obtained within an effective Hamiltonian since they only involve classical susceptibilities. Equation (11) contains two terms. In the first, energy conservation holds for each single $\chi^{(2)}$ process whereas in the second, energy is conserved only for both $\chi^{(2)}$ processes combined.

## 5. Simulation Results for the Three-Level Model

To illustrate the difference between the classical and quantum response of matter, we have calculated them for the three-level scheme shown in Figure 1b and a length L of 10 μm for the nonlinear medium. We assume a rectangular spectral envelope of the probe field with a center frequency of $\omega_c/(2\pi) = 255$ THz and a spectral width of $€\omega/(2\pi) = 150$ THz. Therefore, the probe is off-resonant with respect to both transition frequencies while the THz vacuum can include frequencies resonant with the $g \to g'$ transition. **Figure 4**a depicts the normally ordered second moment $°C$ in Equation (6) together with its three components: the classical response $°C_I$, the response described by the quantum susceptibilities $°C_{II}$ and the response according to the cascading processes $°C_{III}$. $°C_I$ samples the THz vacuum fluctuations which are uncorrelated with the shot noise of the probe. Therefore, it can only enhance the fluctuations of the electro-optic signal. In contrast, both quantum corrections can also lead to a reduction of the noise due to the effective interaction between the molecules mediated by the THz vacuum. Interestingly, there are certain phase shifts θ where one of the three contributions is dominant. Figure 4a,c demonstrate that for a quarter-wave plate ($\theta = \pi/2$) the quantum contributions are small compared to the classical response while for a half-wave plate ($\theta = \pi$), the quantum contribution $°C_{II}$ constitutes almost the entire electro-optic signal. Outcomes for intermediate phase shifts are dominated by the cascading contribution $°C_{III}$. The fact that both the classical and the cascading contributions almost vanish in the half-wave plate configuration ($\theta = \pi$) is remarkable and suggests that electro-optic sampling could also be used as a spectroscopic tool to study the pure quantum susceptibilities of different materials.

As demonstrated in Figure 4b, the quantum susceptibilities involved in the gating function D_q almost vanish in the off-resonant case. However, the cascading processes[36] described by the gating function D_{casc} still constitute a significant contribution even if all fields involved are off resonance with respect to the transition frequencies of the material. Figure 4b shows the off-resonant normally-ordered second moment $°C$ in Equation (6) where we have now assumed a three-level model with transition frequencies $\omega, \ll \omega'_{g'g}, \omega'_{fg}$. The cascading processes can lead to substantial corrections for intermediate phase shifts of $\pi/2 < \theta < \pi$ and $\pi < \theta < 3\pi/2$. These corrections are given by the second term in Equation (11). They are thus originating from processes where an energy excess or deficiency is created in the first $\chi^{(2)}$ process only to be compensated by the second $\chi^{(2)}$ process. This exchange of energy between the two nonlinear steps can only happen within a certain distance determined by the frequency of the generated THz field. This fact also explains why the second term in Equation (11) scales just linearly with the length of crystal. The presence of this effect is therefore owed to the short length of the crystal and the broadband nature of the sampling.

In previous experiments,[21,22] electro-optic sampling was carried out with a phase shift of $\theta = \pi/2$. Interestingly, Figure 4b shows that while the cascading processes result in distinct contributions for various phase shifts, they can be neglected and thus remain hidden in this configuration so that the classical treatment provides a good approximation. However, their presence can be inferred, for example, if spectral filtering is introduced into the measurement according to **Figure 5**a where only half of

**ADVANCED
SCIENCE NEWS**

www.advancedsciencenews.com

LASER
& PHOTONICS
REVIEWS

www.lpr-journal.org

Figure 4. Normally-ordered second moment ff of the electro-optic signal calculated according to Equations (7), (9), and (11) for different phase shifts θ. a) ff according to the level scheme shown in Figure 1b. The blue line depicts ff for the full quantum treatment given by Equation (6). It is given by the sum of the classical contribution ff_I [black line, cf. Equation (7)], the contribution stemming from the quantum susceptibilities ff_{II} [dashed orange line, cf. Equation (9)] and the cascading contribution ff_{III} [dashed green line, cf. Equation (11)]. b) Off-resonant case with $\omega, \ll \omega'_{g'g}, \omega'_{fg}$. The length L of the nonlinear medium with respect to the strength of the nonlinear susceptibilities is chosen such that the maximal value of ff can still be regarded as a small correction to the shot noise. In this case, a maximum contribution of $0.2N$ was adopted. c) Ratio of the absolute strength of the quantum contribution $|ff_{II}|$ to the combined absolute strengths of each contribution $G = |ff_I| + |ff_{II}| + |ff_{III}|$ for the level scheme shown in Figure 1b. The normally-ordered second moment ff is almost entirely determined by the quantum contribution ff_{II} for the half-wave plate configuration, given by $\theta = \pi$.
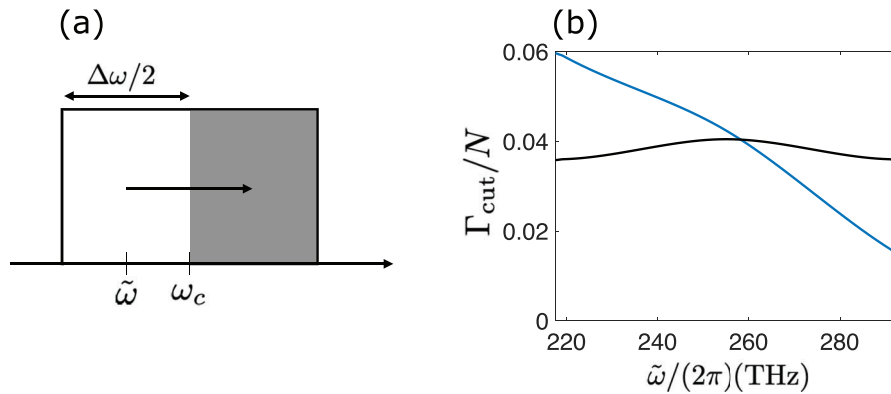
Figure 5. Spectral filtering in electro-optic sampling and effects of the cascading processes. a) Spectral filtering in the gating function. For $\tilde{\omega}/(2\pi) = 217.5$ THz, the lower half of the probe spectrum is detected while $\tilde{\omega}/(2\pi) = 292.5$ THz constitutes a measurement of the upper half of the probe spectrum. b) Comparison of the normally-ordered second moment ff according to Equation (13) between the classical treatment (black line), where only ff_I is taken into account, and the full quantum treatment (blue line) involving also the cascading processes.

the probe spectrum is exploited for detection. The corresponding electro-optic signal is given by
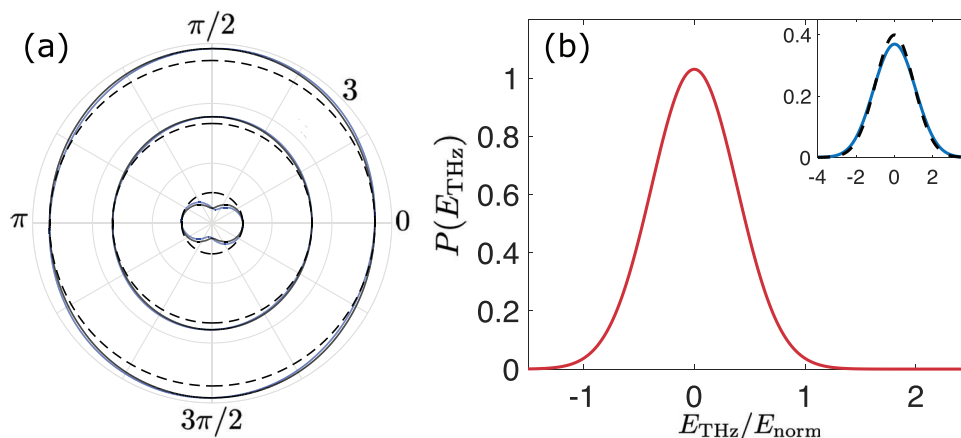
$$\hat{S}_{\text{cut}}(\tilde{\omega}) = C \int_{\tilde{\omega}-\epsilon\omega/4}^{\tilde{\omega}+\epsilon\omega/4} d\omega \frac{1}{\hbar\omega} \left[i\hat{E}_{p,z}^\dagger(\omega)\hat{E}_{p,s}(\omega) + \text{H.c.} \right] \quad (13)$$

where the frequency window is centered at $\tilde{\omega}$. Figure 5a depicts the spectral cut for $\tilde{\omega} = \omega_c - \epsilon\omega/4$, which generally begins in the lower half of the probe spectrum at $\tilde{\omega} - \epsilon\omega/4$ and ends in the upper half at $\tilde{\omega} + \epsilon\omega/4$. Figure 5b illustrates how the normally-ordered second moment °C based on Equation (13) changes upon varying the position of $\tilde{\omega}$. To gain an additional insight, we now compare °C to the case when the cascading processes are excluded from the calculation. Note that these contributions add noise in the lower half of the probe spectrum while subtracting noise in the upper half. The corresponding contributions are cancelled out almost completely when the entire probe spectrum is detected.

We next use the results for °C to calculate the first correction due to the THz field to the probability distribution in Equation (2), which is given by

$$P(S, \theta) = \frac{1}{\sqrt{2\pi N}} \exp\left(-\frac{S^2}{2N}\right)\left(1 + \frac{1}{2N^2}\left(S^2 - N\right) °C\right) \quad (14)$$

The correction to the bare probability distribution of the probe is represented by a single-photon state of the $\vec{e}_s$-polarized NIR field scaling linearly with the normally-ordered second moment of the electro-optic signal °C in Equation (6). **Figure 6**a compares the contour plot of the probability distribution in Equation (14) to that for the bare shot noise of the probe and the probability distribution obtained by only considering the classical contribution $°C_I$. Here, the polar angle does not represent θ, which corresponds to the phase shift induced by the waveplate shown in Figure 1a, but rather the corresponding phase shift $\varphi = \arccos(\sqrt{-\cos\theta})$ induced in the electro-optic signal itself, which is given by $e^{i\varphi(\theta)} = P(\theta)$ [cf. Equation (1)]. The noise added by the classical contribution $°C_I$ turns the rotationally symmetric

ADVANCED
SCIENCE NEWS

www.advancedsciencenews.com

LASER
& PHOTONICS
REVIEWS

www.lpr-journal.org

Figure 6. Statistics of the measured electro-optic signal $\hat{S}(\theta)$ [cf. Equation (1)] and reconstructed statistics of the THz vacuum. a) Contour plot of the probability distribution of the electro-optic signal $\hat{S}(\theta(\varphi))$. The blue line depicts the probability distribution according to Equation (6), the black line shows the probability distribution resulting from the classical treatment, and the black dashed line depicts the probability distribution of the shot noise of the probe. b) Reconstructed statistics of the THz vacuum with $E_{norm} = \frac{c_0}{L\omega_p \chi^{(2)}_{+--}}$. Note that the nonlinearity is independent of the frequency entries in the off-resonant case and can be treated as a constant prefactor. The blue line in the inset depicts the probability distribution of $\hat{S}(\theta = \pi/2)$ and the dashed black line corresponds to the shot noise of the probe. Deconvolution of the two should provide the statistics of the THz vacuum.

probability distribution for the shot noise of the probe into an ellipse with the long axis along the direction of $\varphi = \pi/2$. The quantum correction given mainly by the cascading processes $°C_{III}$ then rotates the long axis of this ellipse and squeezes the generated NIR field $\hat{E}_{p,s}$ for phase shifts of $0.8\pi \lesssim \varphi \leq \pi$.

Ellipsometry enables a full tomography of the generated NIR field $\hat{E}_{p,s}$, as in standard balanced homodyne detection.[37] We now discuss whether the statistics of the THz field itself can be reconstructed from the statistics of the generated NIR field. Figure 6b shows this type of reconstruction for a phase shift of $\varphi = \pi/2$. In this case, the quantum corrections to $°C$ are negligible and the fluctuations added on top of the shot noise are mainly given by the classical contribution $°C_I$ which samples the fluctuations of the THz field and is therefore uncorrelated with the shot noise. Here, the probability distribution of the THz input is given by a simple deconvolution of the probability distribution in Equation (14) with the Gaussian probability distribution for the shot noise of the probe. In contrast, the quantum correction dominated by the cascading processes $°C_{III}$ introduces an additional contribution for other phase shifts that is independent on the state of the THz field and cannot be understood as simply sampling the THz vacuum fluctuations. The cascading processes lead to interference with the $\vec{e}_s$-polarized NIR field $\hat{E}_{p,s}$ and therefore with the shot noise. A simple deconvolution of the probability distribution for the corresponding phase shifts φ would fail to give the correct statistics of the THz vacuum.

6. Conclusion

We have employed the superoperator formalism to develop a microscopic theory for time-domain electro-optic sampling of electric field fluctuations. Three contributions to the electro-optic signal variance were identified: a classical contribution reproducing the results of previous theoretical models[29] and two quantum responses. One part originates from a contribution

stemming from quantum susceptibilities and another one from cascaded nonlinear processes. The quantum corrections strongly depend on the intermolecular time-ordering of the THz interactions in the $\chi^{(2)}$ processes. Here, an effective interaction between the molecules mediated by the THz vacuum fluctuations is established. To demonstrate the difference between the classical and quantum responses, we compared the respective phase-dependent electro-optic contributions for an effective nonlinear medium described by a system of three-level noninteracting molecules. For a configuration involving a quarter-wave plate, we found that the quantum corrections to the normally-ordered second moment of the electro-optic signal vanish. In this case, the electro-optic signal is described by the conventional response also used for classical electro-optic sampling. For other phase shifts, however, the quantum response significantly influences the measured statistics and can also lead to a reduction of the fluctuations below the shot-noise limit of the probe field. For the configuration with a half-wave plate, the classical as well as the cascading processes can be suppressed completely, opening up the possibility to use electro-optic sampling as a novel spectroscopic tool to study quantum susceptibilities. The contribution due to the cascading processes should already be observable with slight changes in present experimental setups by either introducing spectral filtering or studying the electro-optic signal for certain phase shifts in the ellipsometry part. Finally, we describe how the probability distribution of the THz vacuum can be reconstructed from the one of the electro-optic signal as has been achieved experimentally.[21] We note that a reconstruction for other phase shifts would need to take into account the additional quantum contributions. We have shown that the ellipsometry enables detection of the probability distribution of the generated NIR field for phase shifts within an interval of length π, thus providing a full quantum tomography of its state. A method for reconstructing the statistics of the THz input for arbitrary phase shifts would pave a way for quantum tomography of nonclassical fields with subcycle temporal resolution. Our theory provides a

firm basis for addressing the challenging issue of the extraction of these statistics under realistic experimental conditions.

Supporting Information

Supporting Information is available from the Wiley Online Library or from the author.

Conflict of Interest

The authors declare no conflict of interest.

Data Availability Statement

All study data are included in the article and in the Supporting Information of the article.

[1] W. M. Tolles, J. W. Nibler, J. R. McDonald, A. B. Harvey, *Appl. Spectrosc.* **1977**, *31*, 253.
[2] M. Cho, N. F. Scherer, G. R. Fleming, S. Mukamel, *J. Chem. Phys.* **1992**, *96*, 5618.
[3] D. M. Jonas, *Annu. Rev. Phys. Chem.* **2003**, *54*, 425.
[4] S. Mukamel, *Principles of Nonlinear Optical Spectroscopy*, Oxford University Press, Oxford **1995**.
[5] R. W. Boyd, *Nonlinear Optics (Third Edition)*, Academic Press, Burlington **2008**.
[6] M. O. Scully, M. S. Zubairy, *Quantum Optics*, Cambridge University Press, Cambridge **1997**.
[7] M. Kira, S. W. Koch, R. P. Smith, A. E. Hunter, S. T. Cundiff, *Nat. Phys.* **2011**, *7*, 799.
[8] A. Yabushita, T. Kobayashi, *Phys. Rev. A* **2004**, *69*, 013806.
[9] D. A. Kalashnikov, Z. Pan, A. I. Kuznetsov, L. A. Krivitsky, *Phys. Rev. X* **2014**, *4*, 011049.
[10] S. Mukamel, M. Freyberger, W. Schleich, M. Bellini, A. Zavatta, G. Leuchs, C. Silberhorn, R. W. Boyd, L. L. Sánchez-Soto, A. Stefanov, M. Barbieri, A. Paterova, L. Krivitsky, S. Shwartz, K. Tamasaku, K. Dorfman, F. Schlawin, V. Sandoghdar, M. Raymer, A. Marcus, O. Varnavski, T. Goodson III, Z.-Y. Zhou, B.-S. Shi, S. Asban, M. Scully, G. Agarwal, T. Peng, A. V. Sokolov, Z.-D. Zhang, M. S. Zubairy, I. A. Vartanyants, E. del Valle, F. Laussy, *J. Phys. B: At. Mol. Opt. Phys.* **2020**, *53*, 072002.
[11] C. Silberhorn, *Contemp. Phys.* **2007**, *48*, 143.
[12] P. G. Kwiat, E. Waks, A. G. White, I. Appelbaum, P. H. Eberhard, *Phys. Rev. A* **1999**, *60*, 773.
[13] P. J. Mosley, J. S. Lundeen, B. J. Smith, P. Wasylczyk, A. B. U'Ren, C. Silberhorn, I. A. Walmsley, *Phys. Rev. Lett.* **2008**, *100*, 133601.
[14] P. Sharapova, A. M. Pérez, O. V. Tikhonova, M. V. Chekhova, *Phys. Rev. A* **2015**, *91*, 043816.
[15] O. Roslyak, S. Mukamel, *Mol. Phys.* **2009**, *107*, 265.
[16] K. E. Dorfman, S. Mukamel, *Phys. Rev. A* **2012**, *86*, 023805.
[17] K. E. Dorfman, F. Schlawin, S. Mukamel, *Rev. Mod. Phys.* **2016**, *88*, 045008.
[18] Q. Wu, X. Zhang, *Appl. Phys. Lett.* **1995**, *67*, 3523.
[19] A. Leitenstorfer, S. Hunsche, J. Shah, M. C. Nuss, W. H. Knox, *Appl. Phys. Lett.* **1999**, *74*, 1516.
[20] S. Keiber, S. Sederberg, A. Schwarz, M. Trubetskov, V. Pervak, F. Krausz, N. Karpowicz, *Nat. Photonics* **2016**, *10*, 159.
[21] C. Riek, D. V. Seletskiy, A. S. Moskalenko, J. F. Schmidt, P. Krauspe, S. Eckart, S. Eggert, G. Burkard, A. Leitenstorfer, *Science* **2015**, *350*, 420.
[22] I.-C. Benea-Chelmus, F. F. Settembrini, G. Scalari, J. Faist, *Nature* **2019**, *568*, 202.
[23] M. G. Raymer, J. Cooper, H. J. Carmichael, M. Beck, D. T. Smithey, *J. Opt. Soc. Am. B* **1995**, *12*, 1801.
[24] C. Riek, P. Sulzer, M. Seeger, A. S. Moskalenko, G. Burkard, D. V. Seletskiy, A. Leitenstorfer, *Nature* **2017**, *541*, 376.
[25] T. L. M. Guedes, M. Kizmann, D. V. Seletskiy, A. Leitenstorfer, G. Burkard, A. S. Moskalenko, *Phys. Rev. Lett.* **2019**, *122*, 053604.
[26] M. Kizmann, T. L. M. Guedes, D. V. Seletskiy, A. S. Moskalenko, A. Leitenstorfer, G. Burkard, *Nat. Phys.* **2019**, *15*, 960.
[27] I.-C. Benea-Chelmus, C. Bonzon, C. Maissen, G. Scalari, M. Beck, J. Faist, *Phys. Rev. A* **2016**, *93*, 043812.
[28] S. De Liberato, *Phys. Rev. A* **2019**, *100*, 031801.
[29] A. S. Moskalenko, C. Riek, D. V. Seletskiy, G. Burkard, A. Leitenstorfer, *Phys. Rev. Lett.* **2015**, *115*, 263601.
[30] F. Lindel, R. Bennett, S. Y. Buhmann, *Phys. Rev. A* **2020**, *102*, 041701.
[31] P. Sulzer, K. Oguchi, J. Huster, M. Kizmann, T. L. M. Guedes, A. Liehl, C. Beckh, A. S. Moskalenko, G. Burkard, D. V. Seletskiy, A. Leitenstorfer, *Phys. Rev. A* **2020**, *101*, 033821.
[32] G. Gallot, D. Grischkowsky, *J. Opt. Soc. Am. B* **1999**, *16*, 1204.
[33] P. C. M. Planken, H.-K. Nienhuys, H. J. Bakker, T. Wenckebach, *J. Opt. Soc. Am. B* **2001**, *18*, 313.
[34] P. E. Powers, *Fundamentals of Nonlinear Optics*, Taylor & Francis, Boca Raton, FL **2011**.
[35] F. Lindel, R. Bennett, S. Y. Buhmann, *Phys. Rev. A* **2021**, *103*, 033705.
[36] K. Bennett, S. Mukamel, *J. Chem. Phys.* **2014**, *140*, 044313.
[37] W. P. Schleich, *Quantum Optics in Phase Space*, Wiley-VCH, Berlin **2001**.